Review

Metal–Organic Framework (MOF) Derivatives as Promising Chemiresistive Gas Sensing Materials: A Review

Huijie Wei [1], Huiyan Zhang [1,*], Bing Song [1], Kaiping Yuan [2], Hongbin Xiao [3,*], Yunyi Cao [4] and Qi Cao [1,*]

[1] Key Laboratory of Energy Thermal Conversion and Control of Ministry of Education, School of Energy and Environment, Southeast University, Nanjing 210096, China
[2] Frontier Institute of Chip and System, Fudan University, Shanghai 200438, China
[3] Key Laboratory of Optoelectronic Technology and Systems of Ministry of Education, College of Optoelectronic Engineering, Chongqing University, Chongqing 400044, China
[4] Laundry Appliances Business Division of Midea Group, Wuxi 214028, China
[*] Correspondence: hyzhang@seu.edu.cn (H.Z.); xiaohongbin@cqu.edu.cn (H.X.); qicao@seu.edu.cn (Q.C.)

Abstract: The emission of harmful gases has seriously exceeded relative standards with the rapid development of modern industry, which has shown various negative impacts on human health and the natural environment. Recently, metal–organic frameworks (MOFs)-based materials have been widely used as chemiresistive gas sensing materials for the sensitive detection and monitoring of harmful gases such as NO_x, H_2S, and many volatile organic compounds (VOCs). In particular, the derivatives of MOFs, which are usually semiconducting metal oxides and oxide–carbon composites, hold great potential to prompt the surface reactions with analytes and thus output amplified resistance changing signals of the chemiresistors, due to their high specific surface areas, versatile structural tunability, diversified surface architectures, as well as their superior selectivity. In this review, we introduce the recent progress in applying sophisticated MOFs-derived materials for chemiresistive gas sensors, with specific emphasis placed on the synthesis and structural regulation of the MOF derivatives, and the promoted surface reaction mechanisms between MOF derivatives and gas analytes. Furthermore, the practical application of MOF derivatives for chemiresistive sensing of NO_2, H_2S, and typical VOCs (e.g., acetone and ethanol) has been discussed in detail.

Keywords: MOF derivatives; ZIFs; MIL frameworks; metal oxides; gas sensors; chemiresistors

1. Introduction

With the recent rapid development of cities and industry, volatile organic compounds (VOCs) and other harmful gases are being released at an increasing rate, which upon entry into the air destroys the environmental and ecological balance [1,2]. For example, NO_x causes photochemical smog, SO_2 causes acid rain and haze, and HCHO causes inflammation and cancer, each of which is harmful and has a noticeable impact on human health [3–6]. Sensors, which are monitoring devices that convert monitored information into electrical signals or other information, have many advantages, such as simple operation, facile pretreatment, low cost and real-time detection compared with traditional gas analysis instruments such as gas chromatographs and mass spectrometers [7–12]. In previous studies, electrochemical sensors, optical fiber sensors, and capacitive sensors have been applied for the detection of harmful gases [13–17]. However, these sensors have a series of disadvantages, such as low sensitivity, complex design, and high prices. Chemiresistive gas sensors, as a kind of promising chemical gas sensor, are ohmic contact resistors with two electrodes displaying resistance changes when sensing materials come into contact with the analyte, and the nature of the chemical reaction and the concentration change of the analyte can be inferred by this resistance change [18,19]. Chemiresistive gas sensors avoid the shortcomings of other types of gas sensors commonly used in previous research due to their several advantages, such as having a fast response speed, high sensitivity, easy-to-design

Int. J. Environ. Res. Public Health **2023**, 20, 4388

2 of 14

structure, simple operation, and low price; thus, they have been widely used in recent years. It is important to choose gas sensors that are suitable for the recording and monitoring of chemical stimuli and variations in the environment in order to study the changeable trends of harmful gases and in turn set more effective pollution control plans, control the emissions of gas pollutants, and reduce their negative effects. The microstructure and surface state of sensitive materials can influence the performance of gas sensors. Extraordinary structures can increase the number of surface active sites and accelerate the reaction rates [20–23]. For example, a large contact area caused by hollow or porous structures can increase the degree and rate of chemical reactions. Lee et al. studied the acetone sensing properties of ZnO nanoparticles with different oxygen vacancies [24]. The study showed that the existence of oxygen vacancies brought about an excellent response because controlling the surface defects represented a way to change the sensing properties. O_2 in the air adsorbs on the surface of ZnO nanoparticles and combines with the electrons above to form O_2^-, wherein the oxygen vacancy can be used as an electron donor [25–30]. When the sensor is exposed to acetone, O_2^- reacts with acetone, and the adsorbed electrons are then released back into the conduction band (CB), resulting in the reduction of the depletion layer thickness and resistance. Thus, it is important to choose a suitable sensitive material.

Metal–organic frameworks (MOFs), a burgeoning class of metal-coordinated cationic polymer nanomaterials consisting of metal cation aggregates which are linked by organic ligand molecules or metal cations, have large specific surface areas, tunable and porous structures, and high structural stability. Furthermore, MOFs also show excellent adsorption capacity and low environmental toxicity, making them promising candidates for environmental applications such as adsorption and catalysis [31,32]. However, MOFs are generally electrical insulators with poor conductivity. This greatly hinders their usage for chemiresistive gas sensing materials due to the foreseeable intrinsic low response values. In this case, pristine MOFs have been combined with other conductive materials to form heterostructures, either doped with heteroatoms, or simply calcined at high temperature to generate metal oxide-carbon composites (i.e., MOF derivatives) to improve their sensing performance [33,34]. For example, a uniform three-dimensional MXene/MOF composite, $Ti_3C_2T_X$/ZIF-67/CoV$_2$O$_6$, has been obtained by a co-precipitation reaction, which integrated the conductivity of MXene and the redox activity of the MOF [35]. Generally, MOFs are suitable precursor materials which can be used as an ideal template to synthesize porous metal nano-oxides with an ideal structure. In this regard, their derivatives, such as metal oxides, carbon materials, and their composites, are often used as gas sensing materials due to their high chemical stability, rich structural diversity, large specific surface areas with highly porous structures, considerable temperature resistance, low environmental and physiological toxicity, and many other advantages [19,36–39]. Furthermore, the doping of heteroatoms into MOFs is also a method for improving sensing performance. Doping heteroatoms can reduce the particle size of the sensing material by inducing the formation of oxygen vacancies, increasing the contact area and enhancing the sensing performance [40–43]. In addition, the ion or compound activation centers formed by doping heteroatoms can be used as catalysts in chemical reactions between detected gases and sensing materials, accelerating reactions and improving the selectivity and response speeds of sensing materials at a low temperature. Thus, doping heteroatoms into metal oxide-based sensing materials is beneficial for improving their gas-sensing properties [33–47]. For example, Zhang et al. synthesized Cu–In$_2$O$_3$ hollow nanofibers by doping Cu atoms into In$_2$O$_3$ and used them as H$_2$S-sensing materials. Their study showed that the doping of Cu atoms and the formation of their hollow structure increased the number of active sites, and the small amount of CuO formed by Cu oxidation could combine with In$_2$O$_3$ to synthesize the *p–n* heterojunction, greatly improving selectivity and responsiveness to H$_2$S [48]. In addition, the doped heteroatoms could also accelerate the adsorption and desorption of oxygen to electrons, thus improving response performance [49]. In this paper, we summarize the methods of enhancing the sensing performance of chemiresistive gas

sensors for harmful gases, such as by changing the morphology and structure of MOFs, doping heteroatoms, and other design methods.

2. Sensing Principles of Chemiresistive Gas Sensors

The chemiresistive gas sensor, an important part of the gas analysis system, is an instrument which can determine the concentration and composition of detected gas and convert the obtained chemical information into electrical information [50,51]. Chemiresistive gas sensors are often used to detect inorganic small molecular gases and VOCs. Chemiresistive gas sensors react differently when exposed to different inorganic small molecule gases. If exposed to a gas with strong oxidizing or strong reducing properties, the substances in the sensor and the analyte exchange electrons and holes or form a heterojunction to affect the resistance. If exposed to acid and alkaline gas, the substance in the sensor affects the resistance through the occurring chemical adsorption and chemical reaction with the analyte [52]. VOC detection mostly uses polymer as the gas-sensing material of the chemiresistive gas sensor. If exposed to a non-conductive polymer, the sensitive film begins to expand, the conductive path becomes longer, electron transfer becomes more difficult, and the resistance value increases after the polymer absorbs VOCs. However, the resistance value is changed via electron-hole exchange, forming a heterojunction if exposed to conductive polymers [53–58]. In previous studies, the performance of chemiresistive sensors has usually been evaluated by the following parameters: (1) Response (R): $R = (R_{air} - R_{gas})/R_{gas}$, where R_{gas} and R_{air} are the resistance with and without the presence of gaseous analyte; (2) Sensitivity (S): $S = \delta R/\delta C_t$, where Ct is the concentration of the measured gas; (3) Repeatability: Repeatability is measured by comparing the response of the same device to the same concentration of measured gas for multiple cycles; (4) Stability: Stability refers to testing the gas-sensing performance of the same device to the measured gas after being placed at different times, comparing the change in gas sensitivity with time; (5) Selectivity: Selectivity of the gas sensor is evaluated by comparing the response gap of the same device to different gases with the same concentration.

3. Chemiresistive Gas Sensors Using MOF Derivatives

MOF derivatives-based chemiresistive sensors have attracted wide attention. They could simply be synthesized by thermochemical methods such as pyrolysis, using MOF as the template compromising the different functional units including metal ions and carbon species [59].

3.1. NO$_2$ Sensors

NO$_2$, a kind of hazardous vehicle emission product and combustion product of fossil fuels with an acidic nature, can cause many environmental problems, such as acid rain, photochemical smog, haze, and water eutrophication [60–62]. Thus, it is very important to develop gas sensors with high sensing performance for NO$_2$ detection. Studies to date have shown that nanostructured metal oxides have higher sensing performance for NO$_2$ [63,64]. Ren et al. used a Zn-based zeolitic imidazolate framework (ZIF-8) as a template to synthesize porous ZnO nanocubes for the detection of NO$_2$ (Figure 1a) [65]. The experiment indicated that as the temperature increased, the organic bonds of the compounds were gradually pyrolyzed, the organic ligands were removed, and the metal nodes were oxidized to metal oxides leaving voids, as demonstrated by scanning electron microscopy (SEM) images of ZIF-8 and ZIF-8 derivatives at different pyrolysis temperatures (Figure 1b,c). By comparing the response of ZIF-8 derivatives synthesized at different pyrolysis temperatures to 1 ppm NO$_2$, it was noted that ZIF-8-500 synthesized at the pyrolysis temperature of 500 °C had the highest response (Figure 1e). Previous studies have confirmed that the charge transfer between absorbed gas and the gas sensor may affect the sensing performance of metal oxide gas sensors. When the gas sensor is exposed to NO$_2$, NO$_2$ adsorbs on the material and takes electrons from the CB of ZnO, causing a resistance increase and producing an electron depletion layer (Figure 1f). Porous ZnO

nanocubes inherit the high specific surface area of ZIF-8, and its unique porous hollow polyhedral structure creates numerous gas channels, making it easier for NO_2 to adsorb on its surface and take away electrons. Compared with normal ZnO, porous ZnO nanocubes present high sensitivity and a lower NO_2 detection limit. In addition, the prepared gas sensor exhibits good selectivity for NO_2 compared with other gases (CO, C_2H_5OH, H_2, H_2S, NO, NH_3). This is attributed to the excellent microstructure and surface states of the nanomaterials.
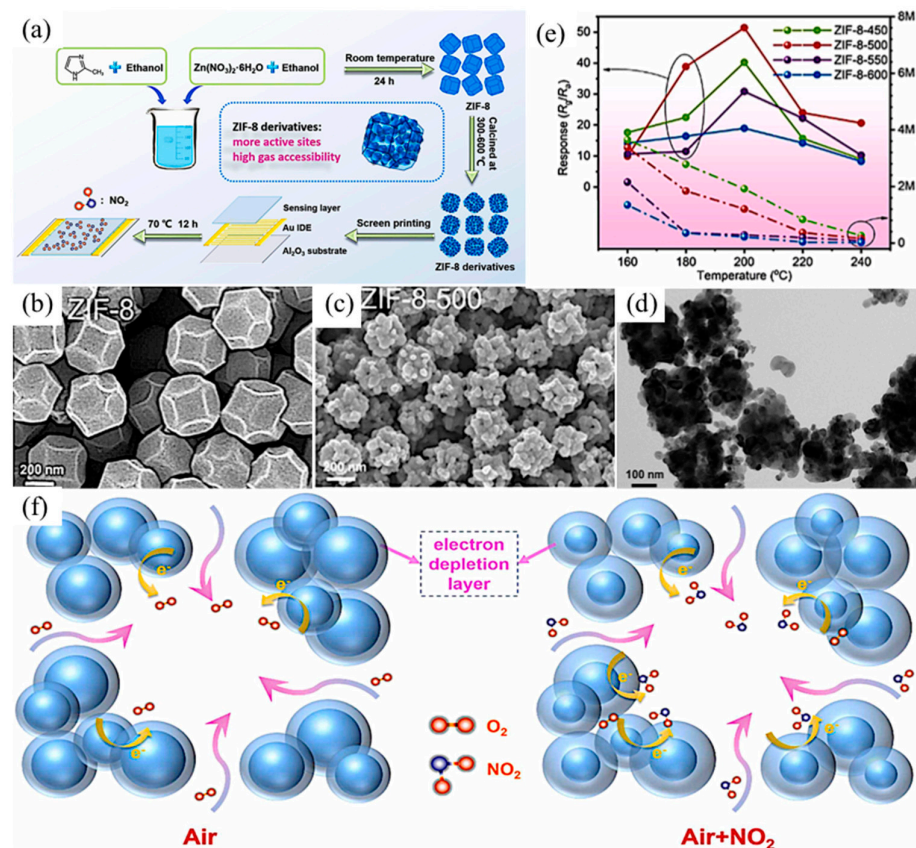
Figure 1. (**a**) Schematics of the synthesis and fabrication process of a ZIF-8 derivatives-based sensor; SEM images of (**b**) ZIF-8 and (**c**) ZIF-8 derivatives after 500 °C pyrolysis; (**d**) TEM images of porous ZIF-8-500; (**e**) Response value to 1 ppm NO_2 at different operating temperatures of ZIF-8-derivatives after different pyrolysis processes; (**f**) Mechanism for the NO_2 sensing process of ZIF-8-500 [65].

Materials Institute Lavoisier (MIL)-based materials synthesized from terephthalic acid and metal-centered octahedron ($MO_4(OH)_2$, M = In, Ga, Fe), which are organic ligands, have a three-dimensional network structure with ultra-high porosity [66]. Du et al. took MIL (M = In) as a precursor doped with a small amount of Fe ions to synthesize $Fe–In_2O_3$ nanorods through thermochemical methods and a pyrolysis process, investigating its NO_2 sensing performance (Figure 2a) [44]. By observing the SEM images of In/Fe-MIL-68s with different levels of Fe(III) content, all the samples showed a hexagonal rod-shaped architecture, the Fe-doped In_2O_3 nanorods had pores on the surface, and the structural size was slightly reduced, which was due to the shrinkage and decomposition of the MOF structure caused by the pyrolysis process. In comparing the high-resolution transmission electron microscopy (HRTEM) images of $Fe(0)–In_2O_3$, it was found that doping Fe(III) forms lattice defects because Fe(III) replaces the In^{3+} ions in the crystal structure (Figure 2d,e). According to Figure 2f,g, $Fe(5)–In_2O_3$ nanorods showed excellent responsiveness and selectivity to NO_2 compared with similar products because the nanorod exhibits superior NO_2 gas-sensing performance at low temperatures due to the high diffusivity, multiple active sites, and wide depletion layer brought by its unique structure. When the sensor

Int. J. Environ. Res. Public Health **2023**, *20*, 4388

5 of 14

is exposed to air, O_2 adsorbs on the surface of the nanorods and extracts the electrons in the sensing material, forming O^- or O^{2-}, which leads to the formation of a potential barrier by bending the energy band and increasing resistance, in turn reflecting the sensing performance of the material for NO_2. When the sensor is exposed to NO_2 gas, it contacts and combines with the electrons of the sensing material to form NO_2^-, resulting in further band bending, higher potential barrier formation, and the further increase in resistance (Figure 2h). In summary, in order to better adsorb and sense the NO_2 molecules, the MOF precursors with high specific surface areas should be selected, and the resulting metal oxide composites are usually doped to improve conductivity, and thereby to improve the electron exchange and sensitivity toward NO_2.
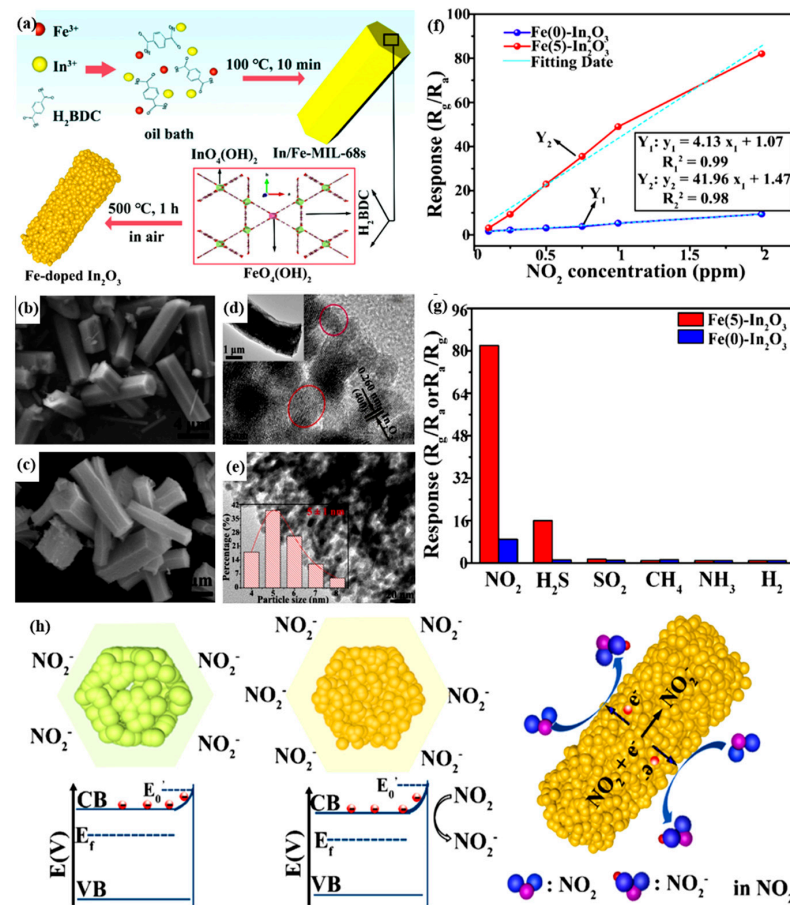

Figure 2. (**a**) Synthetic process of the mesoporous Fe-doped In_2O_3 nanorods derived from In/Fe-MIL-68s; SEM images of (**b**) In/Fe-MIL-68s precursor with 5 mol.% Fe(III) content and (**c**) as-resulted Fe(5)–In_2O_3 nanorods; TEM images of as-resulted (**d**) Fe(0)–In_2O_3 and (**e**) Fe(5)–In_2O_3 porous nanorods; (**f**) Response of Fe(0)–In_2O_3 and Fe(5)–In_2O_3 porous nanorods toward different concentrations of NO_2 at 80 °C; (**g**) Selectivity of the Fe(5)–In_2O_3 sensor toward various tested gases with the concentration of 2 ppm at 80 °C; (**h**) Schematics for the sensing mechanisms of pristine In_2O_3 and Fe-doped In_2O_3 nanorods [44].

With the rapid development of electronic products, wearability and high selectivity have attracted significant attention. In a study by Bag et al., a NO_2 sensor based on reduced graphene oxide (rGO)–$ZnFe_2O_4$ was developed by uniformly anchor smearing MOF-derived mesoporous $ZnFe_2O_4$ microparticles on the rGO sensor layer [67,68]. Because of the synergistic reaction between the mesoporous $ZnFe_2O_4$ particles and the rGO sensing layer, the gas sensor showed improved mechanical stretchability and signal stability compared with rGO-only devices, exhibited superior response and sensitivity to NO_2, and had good

Int. J. Environ. Res. Public Health **2023**, *20*, 4388

6 of 14

repeatability and selectivity even under high humidity conditions, which is expected to be applied in future wearable electronics.
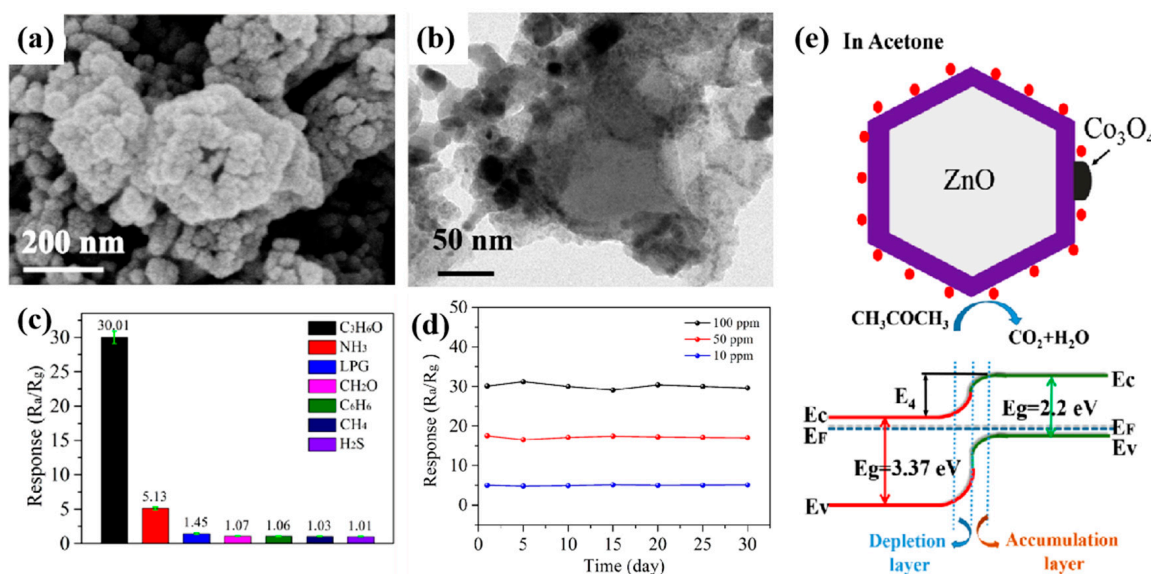
3.2. Acetone Sensors

Acetone, a harmful VOC, is widely used in the chemical industry and chemical experiments. Trace amounts of acetone gas can cause great harm to the environment and to human health, including headache, coma, and even death. Moreover, acetone is one of the important indicators used for diabetes detection [69–71]. Thus, it is very important to develop efficient and sensitive acetone gas sensors. Zhu et al. used Fe-MIL-88B-NH$_2$ as a precursor and MEMS as a substrate to synthesize Fe$_2$O$_3$/C mesoporous nanorods (NR) via simple hydrothermal and pyrolysis reactions, and investigated its acetone-sensing properties [72,73]. The experiment indicated that when the calcination temperature was lower than 500 °C, as the temperature increased, α-Fe$_2$O$_3$ was gradually formed in the compounds, the crystallinity was increased, and the organic molecules were gradually carbonized and decomposed, as shown in the SEM images of the Fe-MOF precursors and their derivatives at different calcination temperatures (Figure 3a,b). Furthermore, the specific surface area of the mesoporous NRs increased significantly after calcination at 300 °C, which was beneficial to their acetone gas-sensing properties. In addition, a hollow structure was formed in the compound, which might have been caused by the lattice rearrangement and the complete decomposition of the organic ligands when the calcination temperature reached 400 °C, as displayed in the TEM images (Figure 3c,d). When the synthesized material was exposed to acetone, the electrons on the Fe$_2$O$_3$ surface were captured by the oxygen adsorbed on it, resulting in an increase in the depletion layer and the potential barrier. The oxygen species adsorbed on its surface reacted with acetone, changing the resistance (Figure 3g). The study showed that the synthesized carbon nanoparticle-modified mesoporous α-Fe$_2$O$_3$ NRs exhibited excellent thermal stability, accurate selectivity, and a fast response to acetone (Figure 3e,f), which may have been due to its large specific surface area and excellent electrical conductivity.
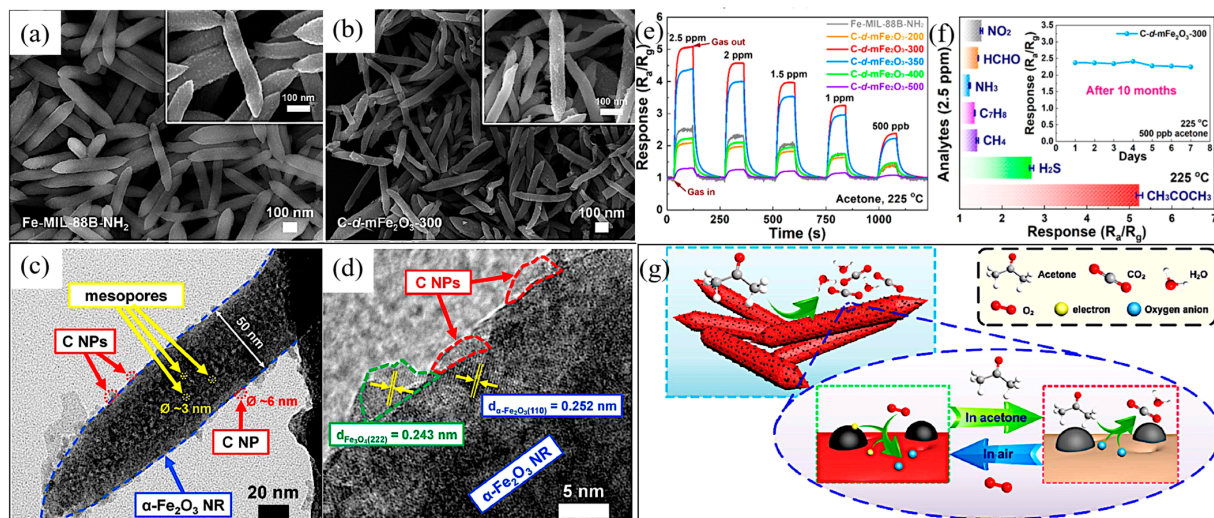
Figure 3. Low- and high-magnification (inset) SEM images of (**a**) Fe-MOF precursor (Fe-MIL-88B-NH$_2$ NRs) and (**b**) MOF-derived products obtained under 300 °C; (**c**) TEM and (**d**) HRTEM images of as-obtained carbon nanoparticles decorated mesoporous α-Fe$_2$O$_3$ NRs (C-d-mFe$_2$O$_3$-300 NRs); (**e**) Dynamic response curves of gas sensors based on Fe-MIL-88B-NH$_2$ and C-d-mFe$_2$O$_3$-*x* (*x* = 200, 300, 350, 400, and 500) NRs facing different concentrations (0.5–2.5 ppm) of acetone at 225 °C; (**f**) Responses of C-d-mFe$_2$O$_3$-300 sensor to various gases including NO$_2$, H$_2$S, NH$_3$, C$_7$H$_8$, CH$_4$, HCHO, and CH$_3$COCH$_3$ with the same concentration of 2.5 ppm; (**g**) Schematic illustration of the acetone sensing process by C-d-mFe$_2$O$_3$-300 NRs [72].

Int. J. Environ. Res. Public Health **2023**, *20*, 4388

7 of 14

Zhang et al. synthesized a ZnO/Co_3O_4 nano-heterostructure using ZIF-8/ZIF-67 as a precursor via a facile co-precipitation method [74]. The experiment results demonstrated that ZnO nanopolyhedrons are composed of many small pores. ZnO/Co_3O_4 nanopolyhedrons exhibit a similar hollow polyhedron structure with ZnO nanopolyhedrons revealed by the SEM and TEM images (Figure 4a,b). The response diagrams of the ZnO and ZnO/Co_3O_4 thin film sensors to acetone were further observed (Figure 4c,d) in the experiment, which showed that the ZnO/Co_3O_4 thin film sensor exhibited good selectivity, reproducibility, repeatability, and stability to acetone. When ZnO is exposed to air, oxygen molecules adsorb on the surface of ZnO nanopolyhedrons and obtain electrons to form O^{2-} and O^{-} ions, forming a further depletion layer. When ZnO was exposed to acetone, the acetone reacted with the adsorbed oxygen ions, thereby reducing the height and width of the depletion layer and further reducing the resistance of the sensor (Figure 4e). The sensing mechanism of the ZnO/Co_3O_4 acetone sensor is similar to that of ZnO, while the sensing performance is greatly improved with regard to response, repeatability, and selectivity. This may be facilitated by the superior catalytic performance of Co_3O_4, the *p–n* heterojunction formed between ZnO and Co_3O_4, and the unique hollow structure. In general, sophisticated metal oxide-based heterostructures with enhanced porosity and lattice rearrangement, or with a favorable *p–n* heterojunction, could be obtained from designed MOFs as the template, which could consequently achieve a rapid response to acetone as a result, being attributable to the improved carrier dynamics [75–78].


Figure 4. SEM (**a**) and TEM (**b**) images of the ZIF-8/ZIF-67-derived ZnO/Co_3O_4 nanopolyhedrons; (**c**) Selectivity of the ZnO/Co_3O_4 nanocomposite sensor; (**d**) Long-term stability over 30 days toward 10, 50, and 100 ppm acetone of the ZnO/Co_3O_4 nanocomposite sensor; (**e**) Schematics of the acetone sensing mechanism of the $ZnO–Co_3O_4$ heterojunction [74].

3.3. Ethanol Sensors

Zhang et al. attempted to synthesize solid, hollow, and hierarchical hollow nanocages with quantum dots (HHQD) of ZnO for ethanol gas sensing [79]. The HHQD-ZnO nanocages were synthesized from the ZIF-8 product with a size of 170 mm (170-ZIF-8) as a precursor, and the SEM images of the 170-ZIF-8 nanocrystals (Figure 5a,b) indicated that the synthesized 170-ZIF-8 precursors had a uniform cage-like morphology with good connectivity between particles. The further study of the TEM images revealed (Figure 5c,d) that the formed HHQD-ZnO nanocages inherited the cage-like morphology of the precursor, presenting a large-area hollow structure and a large specific surface area. According to the response diagram of the HHQD-ZnO nanocages to ethanol gas (Figure 5e), the response value of the HHQD-ZnO nanocage sensor to ethanol was much higher than that of the solid

Int. J. Environ. Res. Public Health **2023**, *20*, 4388

8 of 14

ZnO nanocage sensor, and the sensor showed high selectivity to ethanol gas (Figure 5f), which was due to the unique hollow interpenetrating nanostructure and large specific surface area. When the HHQD-ZnO nanocage sensor was exposed to ethanol, its hollow nanocage structure could adsorb oxygen and carry away free electrons from the CB, thereby increasing the potential barrier and resulting in resistance change.
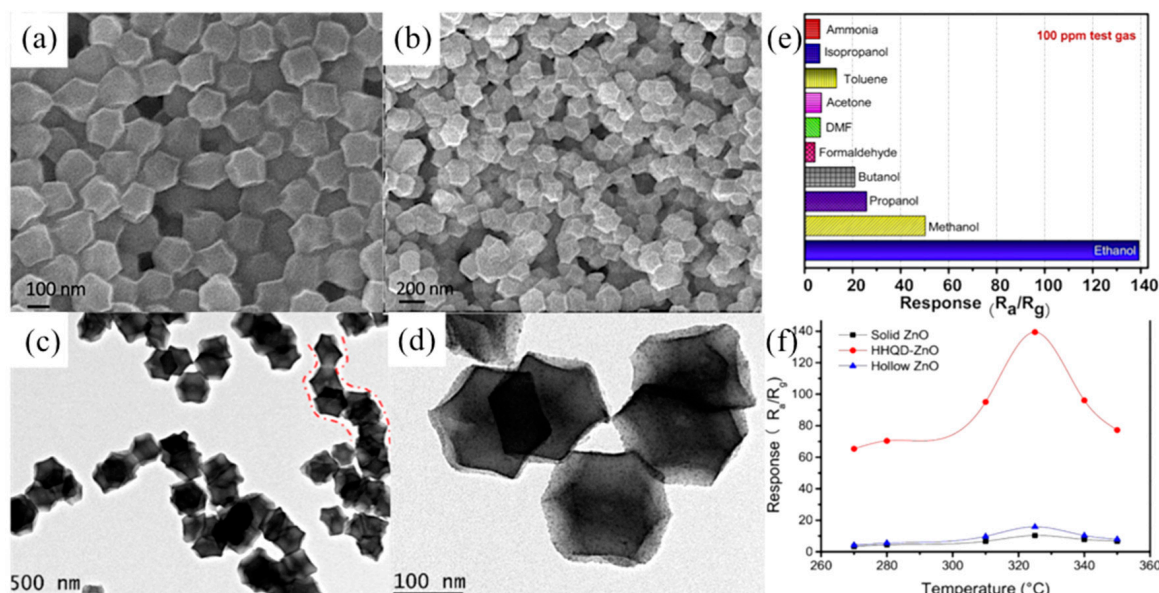

Figure 5. SEM and TEM images of (**a**,**c**) the 170-ZIF-8 precursor and (**b**,**d**) the as-derived HHQD-ZnO nanocage; (**e**) Response of HHQD-ZnO nanocages-based gas sensor toward 100 ppm different target gases (ammonia, formaldehyde, dimethylformamide, acetone, toluene, isopropanol, methanol, propanol, butanol and ethanol, respectively); (**f**) Responses of the sensors based on HHQD-ZnO, hollow ZnO and solid ZnO to 100 ppm ethanol gas at different operating temperatures [80].

3.4. H_2S Sensors

H_2S is a flammable and toxic gas which can be produced in the production processes of food processing plants, paper mills, oil refineries, and other factories, and can also be produced by gas combustion and after the decomposition of human and animal excreta [80–84]. H_2S can affect the human nervous system and visual system, causing Alzheimer's disease, loss of consciousness, and other problems [85]. Thus, it is urgent that H_2S detection and monitoring sensing systems are improved in order to reasonably control H_2S emissions [86,87]. Li et al. first synthesized CPP-3 (In) microrods and then used Cu^{2+}-impregnated CPP-3 (In) microrods impregnated with Cu^{2+} as MOF precursors to synthesize bamboo-like CuO/In_2O_3 heterostructures via heating, cooling, centrifugation, drying, and calcination (Figure 6a) [88]. SEM (Figure 6b) and TEM images (Figure 6c) of CuO/In_2O_3 showed that the synthesized CuO/In_2O_3 inherited the rod-like shape of the CPP-3(In) precursor, but the average size was slightly reduced, showing a bamboo-like hollow structure. In addition, the images also showed the existence of *p–n* heterojunctions formed between CuO and In_2O_3 nanoparticles. By comparing the response values of CuO/In_2O_3 to different gases (Figure 6d,e), CuO/In_2O_3 showed excellent selectivity and responsiveness to H_2S at low temperatures. Intrinsically, CuO is a *p*-type compound and In_2O_3 is an *n*-type compound. When CuO came into contact with In_2O_3, holes in the CuO and electrons in the In_2O_3 flowed in opposite directions, forming an internal electric field, an energy band bending in the depletion layer, and subsequently forming a *p–n* heterojunction, enhancing gas-sensing performance (Figure 6f,g). Finally, the unique mesoporous bamboo-like hollow structure and the facilitated electron transfer resulted from the *p–n* heterojunction, and together enabled the CuO/In_2O_3 sensor superior selectivity, reproducibility, and sensitivity to H_2S. Furthermore, Karuppasamy et al. synthesized $Ni_4Mo/MoO_2@C$ composite

nanospheres via a co-precipitation and high-temperature calcination process using MOF as a precursor [89]. The gas response of the Ni_4Mo/MoO_2@C composite nanospheres to H_2S was 3.5 times and 2.6 times higher than those of Ni-MOF and Mo-MOF, respectively, which was attributed to the synergistic effect of the Ni_4Mo/MoO_2@C composite nanospheres and the high surface area derived from the unique morphology. Overall, the *p–n* heterojunction with well-defined energy level bending can be introduced into the depletion layer with the reverse flow of holes and electrons, which could afford a reliable detection of H_2S at a lower power consumption [90–92].
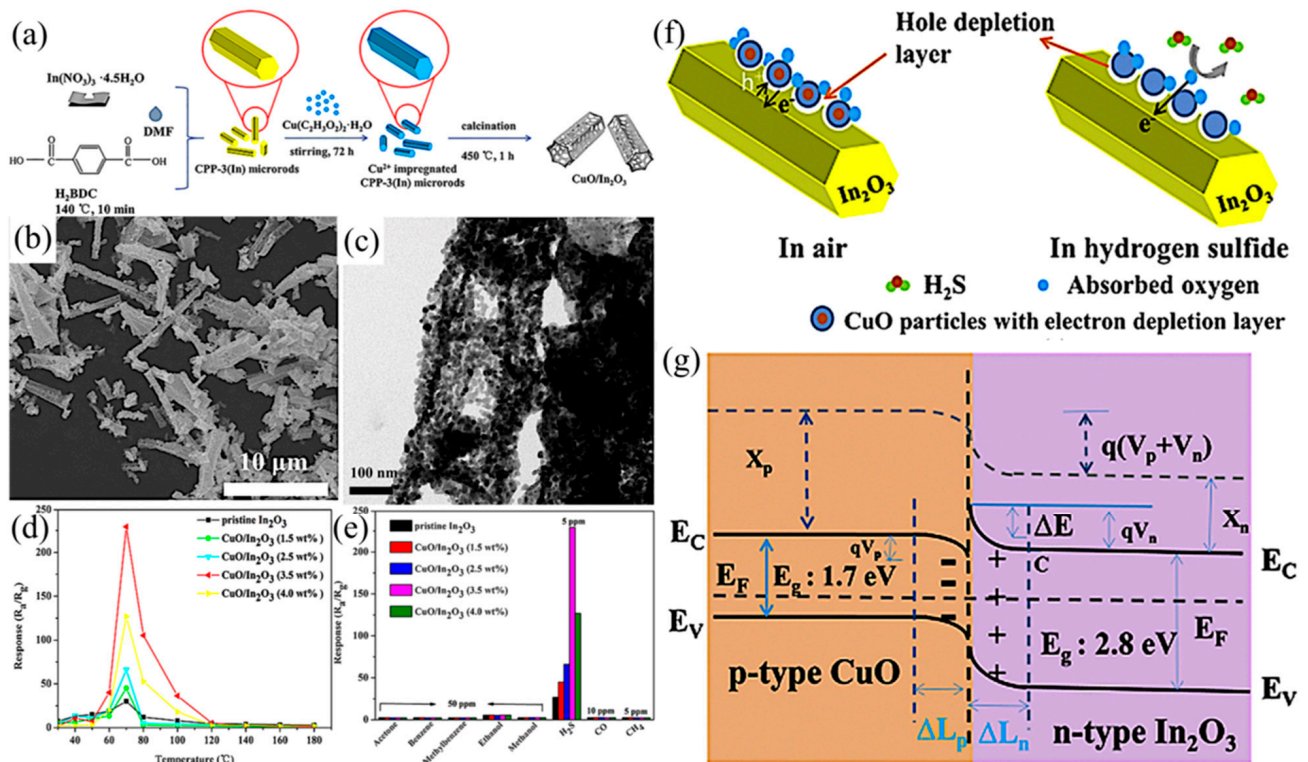
Figure 6. (**a**) Schematic illustration of the formation of CuO/In_2O_3; (**b**) SEM image of as-prepared samples of CuO/In_2O_3 (CuO concentration = 3.5 wt%) and corresponding (**c**) TEM image; (**d**) Response of each sensor to 5 ppm H_2S at different operating temperatures; (**e**) Selectivity of each sensor to 5 ppm H_2S gas and other gases (5, 10, or 50 ppm) at 70 °C; (**f**) Schematics of carrier transportation and gas-sensing mechanism of the CuO/In_2O_3 heterostructure; (**g**) Energy level diagram of CuO/In_2O_3 heterostructure [88].

3.5. Other Gas Sensors

Zhang et al. synthesized $NiFe_2O_4$ nano-octahedrons via the direct pyrolysis of NiFe-bimetallic MOFs to explore its gas sensing performance to toluene [93]. The study showed that the sensor exhibited a low recovery time, strong stability, high repeatability, and low detection, which was due to the catalytic properties and high specific surface area resulting from its porous structure. Qin et al. synthesized Co_3O_4 dodecahedrons by calcining a Co-MOF template. The sensing material exhibited good selectivity and high responsiveness to CO because of the large number of Co^{3+} active sites and surface adsorption of oxygen [94].

4. Conclusions and Future Perspectives

The chemiresistors, a type of chemical gas sensor, can detect the concentration changes of target gases through changes in resistance signals. Studies have shown that the performance of chemiresistors could be promoted by selecting suitable gas-sensing materials to achieve high responsiveness and selectivity to the specific target gas. MOF derivatives synthesized with MOFs as precursors hold great potential in gas sensing due to their unique

structures, high selectivity, sensitivity, and versatility. In this review, we summarized the applications of MOF derivatives for sensing NO_2, acetone, ethanol, H_2S, and several other toxic gases, with their detailed sensing performance and mechanisms being described and discussed.

However, although the novel MOF derivatives-based chemiresistors suggest many new opportunities in in situ detection and monitoring of the harmful gases in industries and in daily life, there are still several challenging points which need to be dealt with:

(1). The MOF derivatives should successfully maintain or inherit the original high porosity and redox activity of pristine MOFs during the high-temperature pyrolysis process so that they can achieve excellent sensitivity and response as a chemiresistive gas sensor;

(2). The sophisticated morphologies and precisely tailored physicochemical properties of the MOF derivatives need to be constructed and established by thermochemical or other methods, avoiding from the unfavorable Ostwald ripening process, in order to increase the active surface areas affording adsorption and catalysis reaction with gaseous molecules, and also the surface electron affinity to enhance their resistance changing signals;

(3). Efficient charge transfer needs to be realized by the construction of a *p–n* junction and other heterojunction interfaces so that rapid response and recovery times are available for the chemiresistive gas sensors;

(4). The reproducibility and cost control for the preparation of MOF derivatives and the as-resulted chemiresistive sensing devices are still far from satisfactory;

(5). The realization of self-powered, minimized and potable gas sensing devices based on MOF derivatives is another indispensable future research direction, especially with the rapid development of 5G wireless networks currently taking place;

(6). Finally, the rapid and efficient data transmission and establishment of the gas sensors-based IoT system, which are of great significance to safer and cleaner production by avoiding the leakage of toxic, harmful, flammable and explosive gases like methane leakage during the exploitation of oil and natural gas, also require the further utilization and optimization of the MOF derivatives-based chemiresistive gas sensors.

References

1. Mor, S.; Kumar, S.; Singh, T.; Dogra, S.; Pandey, V.; Ravindra, K. Impact of COVID-19 lockdown on air quality in Chandigarh, India: Understanding the emission sources during controlled anthropogenic activities. *Chemosphere* **2021**, *263*, 127978. [CrossRef] [PubMed]

2. Guo, Y.; Wen, M.; Li, G.; An, T. Recent advances in VOC elimination by catalytic oxidation technology onto various nanoparticles catalysts: A critical review. *Appl. Catal. B Environ.* **2021**, *281*, 119447. [CrossRef]

3. Zhang, L.; Liang, J.; Wang, Y.; Mou, T.; Lin, Y.; Yue, L.; Li, T.; Liu, Q.; Luo, Y.; Li, N.; et al. High-performance electrochemical NO reduction into NH_3 by MoS_2 nanosheet. *Angew. Chem. Int. Ed.* **2021**, *133*, 25467–25472. [CrossRef]

4. Xu, C.; Zhao, W.; Zhang, M.; Cheng, B. Pollution haven or halo? The role of the energy transition in the impact of FDI on SO_2 emissions. *Sci. Total Environ.* **2021**, *763*, 143002. [CrossRef] [PubMed]

5. Hu, W.; Wan, L.; Jian, Y.; Ren, C.; Jin, K.; Su, X.; Bai, X.; Haick, H.; Yao, M.; Wu, W. Electronic noses: From advanced materials to sensors aided with data processing. *Adv. Mater. Technol.* **2019**, *4*, 1800488. [CrossRef]

Int. J. Environ. Res. Public Health **2023**, *20*, 4388

11 of 14

6. Cao, Q.; Che, R.; Chen, N. Facile and rapid growth of Ag$_2$S microrod arrays as efficient substrates for both SERS detection and photocatalytic degradation of organic dyes. *Chem. Commun.* **2014**, *50*, 4931–4933. [CrossRef]

7. Zhang, D.; Fang, Z.; Wang, L.; Yu, H.; Lu, X.; Song, K.; Teng, J.; Yang, W. Controllable growth of single-crystalline zinc oxide nanosheets under ambient condition toward ammonia sensing with ultrahigh selectivity and sensitivity. *J. Adv. Ceram.* **2022**, *11*, 1187–1195. [CrossRef]

8. Cao, Q.; Liu, X.; Yuan, K.; Yu, J.; Liu, Q.; Delaunay, J.J.; Che, R. Gold nanoparticles decorated Ag(Cl, Br) micro-necklaces for efficient and stable SERS detection and visible-light photocatalytic degradation of Sudan I. *Appl. Catal. B Environ.* **2017**, *201*, 607–616. [CrossRef]

9. Cheng, Y.F.; Cao, Q.; Zhang, J.; Wu, T.; Che, R. Efficient photodegradation of dye pollutants using a novel plasmonic AgCl microrods array and photo-optimized surface-enhanced Raman scattering. *Appl. Catal. B Environ.* **2017**, *217*, 37–47. [CrossRef]

10. Cao, Q.; Yuan, K.; Yu, J.; Delaunay, J.J.; Che, R. Ultrafast self-assembly of silver nanostructures on carbon-coated copper grids for surface-enhanced Raman scattering detection of trace melamine. *J. Colloid Interface Sci.* **2017**, *490*, 23–28. [CrossRef]

11. Li, L.; Zou, J.; Han, Y.; Liao, Z.; Lu, P.; Nezamzadeh-Ejhieh, A.; Liu, J.; Peng, Y. Recent advances in Al(III)/In(III)-based MOFs for the detection of pollutants. *New J. Chem.* **2022**, *46*, 19577–19592. [CrossRef]

12. Zhou, S.; Lu, L.; Liu, D.; Wang, J.; Sakiyama, H.; Muddassir, M.; Nezamzadeh-Ejhieh, A.; Liu, J. Series of highly stable Cd(II)-based MOFs as sensitive and selective sensors for detection of nitrofuran antibiotic. *CrystEngComm* **2021**, *23*, 8043–8052. [CrossRef]

13. Kimmel, D.W.; LeBlanc, G.; Meschievitz, M.E.; Cliffel, D.E. Electrochemical sensors and biosensors. *Anal. Chem.* **2012**, *84*, 685–707. [CrossRef] [PubMed]

14. Kim, K.J.; Lu, P.; Culp, J.T.; Ohodnicki, P.R. Metal-organic framework thin film coated optical fiber sensors: A novel waveguide based chemical sensing platform. *ACS Sens.* **2018**, *3*, 386–394. [CrossRef]

15. Surya, S.G.; Bhanoth, S.; Majhi, S.M.; More, Y.D.; Teja, V.M.; Chappanda, K.N. A silver nanoparticle-anchored UiO-66 (Zr) metal-organic framework (MOF)-based capacitive gas sensor. *CrystEngComm* **2019**, *21*, 7303–7312. [CrossRef]

16. Cao, Q.; Yuan, K.; Liu, Q.; Liang, C.; Wang, X.; Cheng, Y.F.; Li, Q.; Wang, M.; Che, R. Porous Au–Ag alloy particles inlaid AgCl membranes as versatile plasmonic catalytic interfaces with simultaneous, in situ SERS monitoring. *ACS Appl. Mater. Interfaces* **2015**, *7*, 18491–18500. [CrossRef]

17. Cao, Q.; Che, R. Tailoring Au–Ag–S composite microstructures in one-pot for both SERS detection and photocatalytic degradation of plasticizers DEHA and DEHP. *ACS Appl. Mater. Interfaces* **2014**, *6*, 7020–7027. [CrossRef]

18. Yao, M.S.; Li, W.H.; Xu, G. Metal–organic frameworks and their derivatives for electrically-transduced gas sensors. *Coord. Chem. Rev.* **2021**, *426*, 213479. [CrossRef]

19. Wang, X.F.; Song, X.Z.; Sun, K.M.; Cheng, L.; Ma, W. MOFs-derived porous nanomaterials for gas sensing. *Polyhedron* **2018**, *152*, 155–163. [CrossRef]

20. Cao, Q.; Zhang, J.; Zhang, H.; Xu, J.; Che, R. Dual-surfactant templated hydrothermal synthesis of CoSe$_2$ hierarchical microclews for dielectric microwave absorption. *J. Adv. Ceram.* **2022**, *11*, 504–514. [CrossRef]

21. Cao, Q.; Hao, S.; Wu, Y.; Pei, K.; You, W.; Che, R. Interfacial charge redistribution in interconnected network of Ni$_2$P–Co$_2$P boosting electrocatalytic hydrogen evolution in both acidic and alkaline conditions. *Chem. Eng. J.* **2021**, *424*, 130444. [CrossRef]

22. Cao, Q.; Yu, J.; Yuan, K.; Zhong, M.; Delaunay, J.J. Facile and large-area preparation of porous Ag$_3$PO$_4$ photoanodes for enhanced photoelectrochemical water oxidation. *ACS Appl. Mater. Interfaces* **2017**, *9*, 19507–19512. [CrossRef] [PubMed]

23. Bian, Y.; Zhang, C.; Wang, H.; Cao, Q. Degradable nanofiber for eco-friendly air filtration: Progress and perspectives. *Sep. Purif. Technol.* **2023**, *306*, 122642. [CrossRef]

24. Lee, J.; Choi, Y.; Park, B.J.; Han, J.W.; Lee, H.S.; Park, J.H.; Lee, W. Precise control of surface oxygen vacancies in ZnO nanoparticles for extremely high acetone sensing response. *J. Adv. Ceram.* **2022**, *11*, 769–783. [CrossRef]

25. Xu, J.; Zhang, C. Oxygen vacancy engineering on cerium oxide nanowires for room-temperature linalool detection in rice aging. *J. Adv. Ceram.* **2022**, *11*, 1559–1570. [CrossRef]

26. Hao, S.; Liu, J.; Cao, Q.; Zhao, Y.; Zhao, X.; Pei, K.; Zhang, J.; Chen, G.; Che, R. In-situ electrochemical pretreatment of hierarchical Ni$_3$S$_2$-based electrocatalyst towards promoted hydrogen evolution reaction with low overpotential. *J. Colloid Interface Sci.* **2020**, *559*, 282–290. [CrossRef]

27. Yu, J.; Cao, Q.; Li, Y.; Long, X.; Yang, S.; Clark, J.K.; Nakabayashi, M.; Shibata, N.; Delaunay, J.J. Defect-rich NiCeO$_x$ electrocatalyst with ultrahigh stability and low overpotential for water oxidation. *ACS Catal.* **2019**, *9*, 1605–1611. [CrossRef]

28. Yu, J.; Wang, J.; Long, X.; Chen, L.; Cao, Q.; Wang, J.; Qiu, C.; Lim, J.; Yang, S. Formation of FeOOH nanosheets induces substitutional doping of CeO$_{2-x}$ with high-valence Ni for efficient water oxidation. *Adv. Energy Mater.* **2021**, *11*, 2002731. [CrossRef]

29. Yuan, K.; Cao, Q.; Lu, H.L.; Zhong, M.; Zheng, X.; Chen, H.Y.; Wang, T.; Delaunay, J.J.; Luo, W.; Zhang, L.; et al. Oxygen-deficient WO$_{3-x}$@TiO$_{2-x}$ core-shell nanosheets for efficient photoelectrochemical oxidation of neutral water solutions. *J. Mater. Chem. A* **2017**, *5*, 14697–14706. [CrossRef]

30. Zeng, X.; Zhao, Y.; Hu, X.; Stucky, G.D.; Moskovits, M. Rational component and structure design of noble-metal composites for optical and catalytic applications. *Small Struct.* **2021**, *2*, 2000138. [CrossRef]

31. Wu, Y.; Pang, H.; Liu, Y.; Wang, X.; Yu, S.; Fu, D.; Chen, J.; Wang, X. Environmental remediation of heavy metal ions by novel-nanomaterials: A review. *Environ. Pollut.* **2019**, *246*, 608–620. [CrossRef] [PubMed]

Int. J. Environ. Res. Public Health **2023**, *20*, 4388

12 of 14

32. Tchinsa, A.; Hossain, M.F.; Wang, T.; Zhou, Y. Removal of organic pollutants from aqueous solution using metal organic frameworks (MOFs)-based adsorbents: A review. *Chemosphere* **2021**, *284*, 131393. [PubMed]

33. Koo, W.T.; Jang, J.S.; Kim, I.D. Metal-organic frameworks for chemiresistive sensors. *Chem* **2019**, *5*, 1938–1963. [CrossRef]

34. Zeng, X.; Nie, T.; Zhao, C.; Zhu, G.; Zhang, X.; Yu, R.; Stucky, G.D.; Che, R. Coupling between the 2D "ligand" and 2D "host" and their assembled hierarchical heterostructures for electromagnetic wave absorption. *ACS Appl. Mater. Interfaces* **2022**, *14*, 41235–41245. [CrossRef]

35. Liu, C.; Bai, Y.; Li, W.; Yang, F.; Zhang, G.; Pang, H. In situ growth of three-dimensional MXene/metal–organic framework composites for high performance supercapacitors. *Angew. Chem. Int. Ed.* **2022**, *61*, e2021162822022.

36. Qin, L.; Liang, F.; Li, Y.; Wu, J.; Guan, S.; Wu, M.; Xie, S.; Luo, M.; Ma, D. A 2D porous zinc-organic framework platform for loading of 5-fluorouracil. *Inorganics* **2022**, *10*, 202. [CrossRef]

37. Qin, L.; Li, Y.; Liang, F.; Li, L.; Lan, Y.; Li, Z.; Lu, X.; Yang, M.; Ma, D. A microporous 2D cobalt-based MOF with pyridyl sites and open metal sites for selective adsorption of CO_2. *Microporous Mesoporous Mater.* **2022**, *341*, 112098. [CrossRef]

38. Dong, X.; Li, D.; Li, Y.; Sakiyama, H.; Muddassir, M.; Pan, Y.; Srivastava, D.; Kumar, A. A 3,8-connected Cd(II)-based metal-organic framework as an appropriate luminescent sensor for the antibiotic sulfasalazine. *CrystEngComm* **2022**, *24*, 7157–7165.

39. Cao, Q.; Li, Q.; Pi, Z.; Zhang, J.; Sun, L.W.; Xu, J.; Cao, Y.; Cheng, J.; Bian, Y. Metal–organic-framework-derived ball-flower-like porous Co_3O_4/Fe_2O_3 heterostructure with enhanced visible-light-driven photocatalytic activity. *Nanomaterials* **2022**, *12*, 904. [CrossRef]

40. Lee, C.S.; Li, H.Y.; Kim, B.Y.; Jo, Y.M.; Byun, H.G.; Hwang, I.S.; Abdel-Hady, F.; Wazzan, A.A.; Lee, J.H. Discriminative detection of indoor volatile organic compounds using a sensor array based on pure and Fe-doped In_2O_3 nanofibers. *Sens. Actuators B Chem.* **2019**, *285*, 193–200. [CrossRef]

41. Wei, D.; Jiang, W.; Gao, H.; Chuai, X.; Liu, F.; Liu, F.; Sun, P.; Liang, X.; Gao, Y.; Yan, X.; et al. Facile synthesis of La-doped In_2O_3 hollow microspheres and enhanced hydrogen sulfide sensing characteristics. *Sens. Actuators B Chem.* **2018**, *276*, 413–420. [CrossRef]

42. Shen, J.; Li, F.; Yin, B.; Sun, L.; Chen, C.; Wen, S.; Chen, Y.; Ruan, S. Enhanced ethyl acetate sensing performance of Al-doped In_2O_3 microcubes. *Sens. Actuators B Chem.* **2017**, *253*, 461–469. [CrossRef]

43. Bai, S.; Guo, T.; Zhao, Y.; Sun, J.; Li, D.; Chen, A.; Liu, C.C. Sensing performance and mechanism of Fe-doped ZnO microflowers. *Sens. Actuators B Chem.* **2014**, *195*, 657–666. [CrossRef]

44. Du, W.; Si, W.; Zhao, J.; Wang, F.; Han, Z.; Wang, Z.; Liu, W.; Lu, G.; Liu, J.; Wu, L. Mesoporous Fe-doped In_2O_3 nanorods derived from metal organic frameworks for enhanced nitrogen dioxide detection at low temperature. *Ceram. Int.* **2020**, *46*, 20385–20394. [CrossRef]

45. Yu, J.; Cao, Q.; Qiu, C.; Chen, L.; Delaunay, J.J. Modulating Ni/Ce ratio in $Ni_yCe_{100-y}O_x$ electrocatalysts for enhanced water oxidation. *Nanomaterials* **2021**, *11*, 437. [CrossRef]

46. Cao, Q.; Yu, J.; Cao, Y.; Delaunay, J.J.; Che, R. Unusual effects of vacuum annealing on large-area Ag_3PO_4 microcrystalline film photoanode boosting cocatalyst- and scavenger-free water splitting. *J. Mater.* **2021**, *7*, 929–939. [CrossRef]

47. Li, Q.; Huang, Z.; Guan, P.; Su, R.; Cao, Q.; Chao, Y.; Shen, W.; Guo, J.; Xu, H.; Che, R. Simultaneous Ni doping at atom scale in ceria and assembling into well-defined lotuslike structure for enhanced catalytic performance. *ACS Appl. Mater. Interfaces* **2017**, *9*, 16243–16251. [CrossRef]

48. Zhang, Y.; Han, S.; Wang, M.; Liu, S.; Liu, G.; Meng, X.; Xu, Z.; Wang, M.; Qiao, G. Electrospun Cu-doped In_2O_3 hollow nanofibers with enhanced H_2S gas sensing performance. *J. Adv. Ceram.* **2022**, *11*, 427–442. [CrossRef]

49. Zhang, C.; Huan, Y.; Li, Y.; Luo, Y.; Debliquy, M. Low concentration isopropanol gas sensing properties of Ag nanoparticles decorated In_2O_3 hollow spheres. *J. Adv. Ceram.* **2022**, *11*, 379–391. [CrossRef]

50. Zhang, M.; Liu, K.; Zhang, X.; Wang, B.; Xu, X.; Du, X.; Yang, C.; Zhang, K. Interfacial energy barrier tuning of hierarchical Bi_2O_3/WO_3 heterojunctions for advanced triethylamine sensor. *J. Adv. Ceram.* **2022**, *11*, 1860–1872. [CrossRef]

51. Yuan, K.; Wang, C.Y.; Zhu, L.Y.; Cao, Q.; Yang, J.H.; Li, X.X.; Huang, W.; Wang, Y.Y.; Lu, H.L.; Zhang, D.W. Fabrication of a micro-electromechanical system-based acetone gas sensor using CeO_2 nanodot-decorated WO_3 nanowires. *ACS Appl. Mater. Interfaces* **2020**, *12*, 14095–14104. [CrossRef] [PubMed]

52. Lonergan, M.; Severin, E.; Doleman, B.; Beaber, S.A.; Grubbs, R.H.; Lewis, N.S. Array-based vapor sensing using chemically sensitive carbon black-polymer resistors. *Chem. Mater.* **1996**, *8*, 2298–2312. [CrossRef]

53. Spitalsky, Z.; Tasis, D.; Papagelis, K.; Galiotis, C. Carbon nanotube-polymer composites: Chemistry, processing, mechanical and electrical properties. *Prog. Polym. Sci.* **2010**, *35*, 357–401. [CrossRef]

54. Yuan, K.; Zhu, L.Y.; Cao, Q.; Ma, H.P.; Tao, J.J.; Huang, W.; Lu, H.L. ALD-based hydrothermal facile synthesis of a dense $WO_3@TiO_2-Fe_2O_3$ nanodendrite array with enhanced photoelectrochemical properties. *J. Mater. Chem C* **2020**, *8*, 6756–6762. [CrossRef]

55. Siahroudi, M.G.; Daryakenari, A.A.; Molamahaleh, Y.B.; Cao, Q.; Daryakenari, M.A.; Delaunay, J.J.; Siavoshi, H.; Molaei, F. Ethylene glycol assisted solvo-hydrothermal synthesis of $NGr-Co_3O_4$ nanostructures for ethanol electrooxidation. *Int. J. Hydrogen Energy* **2020**, *45*, 30357–30366. [CrossRef]

56. Liu, Q.; Cao, Q.; Bi, H.; Liang, C.; Yuan, K.; She, W.; Yang, Y.; Che, R. $CoNi@SiO_2@TiO_2$ and $CoNi@air@TiO_2$ microspheres with strong wideband microwave absorption. *Adv. Mater.* **2016**, *28*, 486–490. [CrossRef]

57. Hao, S.; Cao, Q.; Yang, L.; Che, R. Morphology-optimized interconnected Ni_3S_2 nanosheets coupled with $Ni(OH)_2$ nanoparticles for enhanced hydrogen evolution reaction. *J. Alloys Compd.* **2020**, *827*, 154163. [CrossRef]

58. Yuan, K.; Cao, Q.; Li, X.; Chen, H.Y.; Deng, Y.; Wang, Y.Y.; Luo, W.; Lu, H.L.; Zhang, D.W. Synthesis of $WO_3@ZnWO_4@ZnO$-ZnO hierarchical nanocactus arrays for efficient photoelectrochemical water splitting. *Nano Energy* **2017**, *41*, 543–551. [CrossRef]

59. Yin, Z.; Wan, S.; Yang, J.; Kurmoo, M.; Zeng, M.H. Recent advances in post-synthetic modification of metal-organic frameworks: New types and tandem reactions. *Coord. Chem. Rev.* **2019**, *378*, 500–512. [CrossRef]

60. Agrawal, A.V.; Kumar, N.; Kumar, M. Strategy and future prospects to develop room-temperature recoverable NO_2 gas sensor based on two-dimensional molybdenum sulfide. *Nano-Micro Lett.* **2021**, *13*, 38. [CrossRef]

61. Bauwens, M.; Compernolle, S.; Stavrakou, T.; Müller, J.F.; van Gent, J.; Eskes, H.; Levelt, P.F.; van der A, R.; Veefkind, J.P.; Vlietinck, J.; et al. Impact of coronavirus outbreak on NO_2 pollution assessed using TROPOMI and OMI observations. *Geophys. Res. Lett.* **2020**, *47*, e2020GL087978. [CrossRef] [PubMed]

62. Muhammad, S.; Long, X.; Salman, M. COVID-19 pandemic and environmental pollution: A blessing in disguise? *Sci. Total Environ.* **2020**, *728*, 138820. [CrossRef] [PubMed]

63. Tan, J.; Hussain, S.; Ge, C.; Wang, M.; Shah, S.; Liu, G.; Qiao, G. ZIF-67 MOF-derived unique double-shelled $Co_3O_4/NiCo_2O_4$ nanocages for superior gas-sensing performances. *Sens. Actuators B Chem.* **2020**, *303*, 127251. [CrossRef]

64. Drobek, M.; Kim, J.H.; Bechelany, M.; Vallicari, C.; Julbe, A.; Kim, S.S. MOF-based membrane encapsulated ZnO nanowires for enhanced gas sensor selectivity. *ACS Appl. Mater. Interfaces* **2016**, *8*, 8323–8328. [CrossRef]

65. Ren, X.; Xu, Z.; Liu, D.; Li, Y.; Zhang, Z.; Tang, Z. Conductometric NO_2 gas sensors based on MOF-derived porous ZnO nanoparticles. *Sens. Actuators B Chem.* **2022**, *357*, 131384. [CrossRef]

66. Volkringer, C.; Meddouri, M.; Loiseau, T.; Guillou, N.; Marrot, J.; Férey, G.; Haouas, M.; Taulelle, F.; Audebrand, N.; Latroche, M. The Kagomé topology of the gallium and indium metal-organic framework types with a MIL-68 structure: Synthesis, XRD, solid-state NMR characterizations, and hydrogen adsorption. *Inorg. Chem.* **2008**, *47*, 11892–11901. [CrossRef]

67. Bag, A.; Kumar, M.; Moon, D.B.; Hanif, A.; Sultan, M.J.; Yoon, D.H.; Lee, N.E. A room-temperature operable and stretchable NO_2 gas sensor composed of reduced graphene oxide anchored with MOF-derived $ZnFe_2O_4$ hollow octahedron. *Sens. Actuators B Chem.* **2021**, *346*, 130463. [CrossRef]

68. Li, C.; Cao, Q.; Wang, F.; Xiao, Y.; Li, Y.; Delaunay, J.J.; Zhu, H. Engineering graphene and TMDs based van der Waals heterostructures for photovoltaic and photoelectrochemical solar energy conversion. *Chem. Soc. Rev.* **2018**, *47*, 4981–5037. [CrossRef]

69. Liu, M.; Wang, Z.; Song, P.; Yang, Z.; Wang, Q. Flexible MXene/rGO/CuO hybrid aerogels for high performance acetone sensing at room temperature. *Sens. Actuators B Chem.* **2021**, *340*, 129946. [CrossRef]

70. Parmar, B.; Bisht, K.K.; Rachuri, Y.; Suresh, E. Zn(II)/Cd(II) based mixed ligand coordination polymers as fluorosensors for aqueous phase detection of hazardous pollutants. *Inorg. Chem. Front.* **2020**, *7*, 1082–1107. [CrossRef]

71. Ma, X.; Zhou, X.; Gong, Y.; Han, N.; Liu, H.; Chen, Y. MOF-derived hierarchical $ZnO/ZnFe_2O_4$ hollow cubes for enhanced acetone gas-sensing performance. *RSC Adv.* **2017**, *7*, 34609–34617. [CrossRef]

72. Zhu, L.Y.; Yuan, K.; Li, Z.C.; Miao, X.Y.; Wang, J.C.; Sun, S.; Devi, A.; Lu, H.L. Highly sensitive and stable MEMS acetone sensors based on well-designed α-Fe_2O_3/C mesoporous nanorods. *J. Colloid Interface Sci.* **2022**, *622*, 156–168. [CrossRef] [PubMed]

73. Zhu, L.Y.; Miao, X.Y.; Ou, L.X.; Mao, L.W.; Yuan, K.; Sun, S.; Devi, A.; Lu, H.L. Heterostructured α-$Fe_2O_3@ZnO@ZIF$-8 core-shell nanowires for a highly selective MEMS-based ppb-level H_2S gas sensor system. *Small* **2022**, *18*, 2204828. [CrossRef]

74. Zhang, D.; Yang, Z.; Wu, Z.; Dong, G. Metal-organic frameworks-derived hollow zinc oxide/cobalt oxide nanoheterostructure for highly sensitive acetone sensing. *Sens. Actuators B Chem.* **2019**, *283*, 42–51. [CrossRef]

75. Bayan, E.M.; Petrov, V.V.; Volkova, M.G.; Storozhenko, V.Y.; Chernyshev, A.V. SnO_2–ZnO nanocomposite thin films: The influence of structure, composition and crystallinity on optical and electrophysical properties. *J. Adv. Dielectr.* **2021**, *11*, 2160008. [CrossRef]

76. Uddin, M.F.; Ullah, M.S.; Hoque, S.M.; Khan, F.A.; Momin, A.A.; Islam, S.R.; Salehin, F.; Hakim, M.A. Electrical transport properties of V_2O_5-added Ni–Co–Zn ferrites. *J. Adv. Dielectr.* **2021**, *11*, 2150025. [CrossRef]

77. Guerra, J.D.S.; Guarany, C.A.; Lima, E.C.; Araújo, E.B.; Garcia, J.E. Exploring the electromechanical response and electric field-induced dielectric anomalies in PMN–PT electroceramics. *J. Adv. Dielectr.* **2021**, *11*, 2140005. [CrossRef]

78. Manan, A.; Rehman, M.U.; Ullah, A.; Ahmad, A.S.; Iqbal, Y.; Qazi, I.; Khan, M.A.; Shah, H.U.; Wazir, A.H. High energy storage density with ultra-high efficiency and fast charging–discharging capability of sodium bismuth niobate lead-free ceramics. *J. Adv. Dielectr.* **2021**, *11*, 2150018. [CrossRef]

79. Zhang, X.; Lan, W.; Xu, J.; Luo, Y.; Pan, J.; Liao, C.; Yang, L.; Tan, W.; Huang, X. ZIF-8 derived hierarchical hollow ZnO nanocages with quantum dots for sensitive ethanol gas detection. *Sens. Actuators B Chem.* **2019**, *289*, 144–152. [CrossRef]

80. Wang, X.; Li, S.; Xie, L.; Li, X.; Lin, D.; Zhu, Z. Low-temperature and highly sensitivity H_2S gas sensor based on ZnO/CuO composite derived from bimetal metal-organic frameworks. *Ceram. Int.* **2020**, *46*, 15858–15866. [CrossRef]

81. Pan, W.; Zhang, Y.; Yu, S.; Liu, X.; Zhang, D. Hydrogen sulfide gas sensing properties of metal organic framework derived α-Fe_2O_3 hollow nanospheres decorated with $MoSe_2$ nanoflowers. *Sens. Actuators B Chem.* **2021**, *344*, 130221. [CrossRef]

82. Ngoc, T.M.; Van Duy, N.; Hung, C.M.; Hoa, N.D.; Nguyen, H.; Tonezzer, M.; Hieu, N.V. Self-heated Ag-decorated SnO_2 nanowires with low power consumption used as a predictive virtual multisensor for H_2S-selective sensing. *Anal. Chim. Acta* **2019**, *1069*, 108–116. [CrossRef] [PubMed]

Int. J. Environ. Res. Public Health **2023**, *20*, 4388

14 of 14

83. Cao, Q.; Che, R.; Chen, N. Scalable synthesis of Cu_2S double-superlattice nanoparticle systems with enhanced UV/visible-light-driven photocatalytic activity. *Appl. Catal. B Environ.* **2015**, *162*, 187–195. [CrossRef]

84. Cao, Q.; Cheng, Y.F.; Bi, H.; Zhao, X.; Yuan, K.; Liu, Q.; Li, Q.; Wang, M.; Che, R. Crystal defect-mediated band-gap engineering: A new strategy for tuning the optical properties of Ag_2Se quantum dots toward enhanced hydrogen evolution performance. *J. Mater. Chem. A* **2015**, *3*, 20051–20055. [CrossRef]

85. Cheng, J.; Li, C.; Xiong, Y.; Zhang, H.; Raza, H.; Ullah, S.; Wu, J.; Zhang, G.; Cao, Q.; Zhang, D.; et al. Recent advances in design strategies and multifunctionality of flexible electromagnetic interference shielding materials. *Nano-Micro Lett.* **2022**, *14*, 80. [CrossRef] [PubMed]

86. Wan, X.; Wu, L.; Zhang, L.; Song, H.; Lv, Y. Novel metal-organic frameworks-based hydrogen sulfide cataluminescence sensors. *Sens. Actuators B Chem.* **2015**, *220*, 614–621. [CrossRef]

87. Huang, C.; Liu, D.; Wang, D.; Guo, H.; Thomas, T.; Attfield, J.P.; Qu, F.; Ruan, S.; Yang, M. Mesoporous $Ti_{0.5}Cr_{0.5}N$ for trace H_2S detection with excellent long-term stability. *J. Hazard. Mater.* **2022**, *423*, 127193. [CrossRef]

88. Li, S.; Xie, L.; He, M.; Hu, X.; Luo, G.; Chen, C.; Zhu, Z. Metal-organic frameworks-derived bamboo-like CuO/In_2O_3 heterostructure for high-performance H_2S gas sensor with low operating temperature. *Sens. Actuators B Chem.* **2020**, *310*, 127828. [CrossRef]

89. Karuppasamy, K.; Sharma, B.; Vikraman, D.; Lee, J.H.; Islam, M.; Santhoshkumar, P.; Kim, H.S. Metal-organic framework-derived $Ni_4Mo/MoO_2@C$ composite nanospheres as the sensing materials for hydrogen sulfide detection. *J. Alloys Compd.* **2022**, *900*, 163421. [CrossRef]

90. Lyapunov, N.; Suen, C.H.; Wong, C.M.; Tang, X.; Ho, Z.L.; Zhou, K.; Chen, X.X.; Liu, H.M.; Zhou, X.; Dai, J.Y. Ultralow switching voltage and power consumption of GeS_2 thin film resistive switching memory. *J. Adv. Dielectr.* **2021**, *11*, 2150004. [CrossRef]

91. Khatun, N.; Hossain, M.S.; Begum, M.H.A.; Islam, S.; Tanvir, N.I.; Bhuiyan, R.H.; Al-Mamun, M. Effect of sintering temperature on structural, magnetic, dielectric and optical properties of Ni–Mn–Zn ferrites. *J. Adv. Dielectr.* **2021**, *11*, 2150028. [CrossRef]

92. Wang, C.L. Photocatalytic degradations of JWS-type kinetics. *J. Adv. Dielectr.* **2021**, *11*, 2150029. [CrossRef]

93. Zhang, Y.; Jia, C.; Wang, Q.; Kong, Q.; Chen, G.; Guan, H.; Dong, C. MOFs-derived porous $NiFe_2O_4$ nano-octahedrons with hollow interiors for an excellent toluene gas sensor. *Nanomaterials* **2019**, *9*, 1059. [CrossRef]

94. Sun, J.; Wang, Y.; Song, P.; Yang, Z.; Wang, Q. Metal-organic framework-derived Cr-doped hollow In_2O_3 nanoboxes with excellent gas-sensing performance toward ammonia. *J. Alloys Compd.* **2021**, *879*, 160472. [CrossRef]